Optical and Quantum Electronics **29** *(1997) 651–660*

Self-consistent 1-D solution of multiquantum-well laser equations

G. DEBAISIEUX, G. HERVÉ-GRUYER, M. FILOCHE, S. BOUCHOULE, J. F. PALMIER
France Telecom, CNET/PAB, Laboratoire de Bagneux
196 Avenue Henri-Ravera, BP 107, 92225 Bagneux, Cedex, France

Received 12 December 1996; revised and accepted 10 February 1997

This paper presents a self-consistent 1-D multiquantum-well laser simulation in which, for the first time, the Schrödinger equation is solved over the whole quantum-well zone, taking into account well-to-well coupling. The computed light-intensity curve is compared with experimental results for an InGaAs/InGaAsP multiquantum-well laser and also with simplified models. The quantum calculation has an important influence on the carrier density profile in the active region. This results in a significant difference in the estimation of the threshold current with respect to other simplified models.

1. Introduction

Multiquantum-well (MQW) lasers are now considered as key devices in optical telecommunications systems. Numerical simulation at microscopic level may be of great help for the design and optimization of those devices. It requires the solving of a set of coupled equations, which describe the device electrical and optical properties.

This set of equations consists of the Poisson equation, the Schrödinger equation, electrical transport equations, the Helmholtz equation and a photon rate equation for optical properties. Various solutions of that system have been proposed [1, 2] but none of these takes correctly into account Schrödinger global solutions. In some approaches the Schrödinger equation is solved once as a pre-processing step and the discrete levels are calculated with flat bands [1]. In other works, the Schrödinger equation is independently solved in each well [2].

In this paper, a 1-D MQW laser simulation is presented in which the Schrödinger equation is introduced as a full part of the coupled system and globally solved over the entire range of quantum wells in the active layer. The model takes into account such effects as band bending and coupling between wells.

This model is applied to an InGaAs/InGaAsP multiquantum-well laser and experimental L-I curves are compared with the computed one. This model is also compared with the simple model in which the Schrödinger equation is not included in the equation set and carrier densities are calculated everywhere assuming a 3-D density of states.

0306–8919

2. Model

In the steady state, MQW laser physics can be described by the following set of equations.

2.1. Poisson equation

$$\nabla(\varepsilon\nabla\phi) = q(n - p - D) \tag{1}$$

where ε is the permittivity, ϕ the electrostatic potential, q the electron charge, n the electron concentration, p the hole concentration and D the doping concentration.

2.2. Transport equations (drift-diffusion model)

Current densities:

$$\begin{aligned} J_\mathrm{n} &= qn\mu_\mathrm{n}\nabla\phi_\mathrm{n} \\ J_\mathrm{p} &= qp\mu_\mathrm{p}\nabla\phi_\mathrm{p} \end{aligned} \tag{2}$$

Continuity:

$$\begin{aligned} \mathrm{div}\, J_\mathrm{n} &= qU_\mathrm{n} \\ \mathrm{div}\, J_\mathrm{p} &= qU_\mathrm{p} \end{aligned} \tag{3}$$

where J_n is the electron current density and J_p the hole current density, ϕ_n and ϕ_p are the quasi-Fermi levels for electrons and holes, μ_n and μ_p are the carrier mobilities for electrons and holes. The recombination terms U_n and U_p include spontaneous (U_sp), Auger (U_Auger), Schockley–Read–Hall (U_RSH) and stimulated recombinations.

2.3. Carrier densities

Carrier densities are calculated within the parabolic approximation. Two cases are distinguished.

2.3.1. Carrier densities in the quantum-well zone

The quantum-well zone consist of wells and barriers, where the Schrödinger equation is consistently solved over the whole region. Assuming a slowly varying effective mass, a Ben–Daniel–Duke Hamiltonian is used:

$$H = -\frac{\hbar^2}{2}\frac{\partial}{\partial z}\frac{1}{m(z)}\frac{\partial}{\partial z} + \phi(z) \tag{4}$$

where m is the particle effective mass. The Schrödinger equation is solved twice, once for electrons in the conduction band and once for holes in the valence band. When the discrete energy levels E_i and wavefunctions ψ_i are known, carrier densities are given by:

$$\begin{aligned} n(z) = {} & \frac{k_\mathrm{b}Tm_\mathrm{e}(z)}{\pi\hbar^2}\sum_i |\psi_i^\mathrm{e}(z)|^2 \log\left(1 + \exp\left(\frac{\phi_\mathrm{n}(z) - E_i^\mathrm{e}}{k_\mathrm{B}T}\right)\right) + N_\mathrm{c}(z)\mathscr{F}_{1/2}\left(\frac{\phi_\mathrm{n}(z) + \phi(z) - \chi_\mathrm{b}}{k_\mathrm{B}T}\right) \\ p(z) = {} & \frac{k_\mathrm{b}Tm_\mathrm{h}(z)}{\pi\hbar^2}\sum_i |\psi_i^\mathrm{h}(z)|^2 \log\left(1 + \exp\left(\frac{E_i^\mathrm{h} - \phi_\mathrm{p}(z)}{k_\mathrm{B}T}\right)\right) \\ & + N_\mathrm{v}(z)\mathscr{F}_{1/2}\left(\frac{-\phi(z) + \chi_\mathrm{b} - E_\mathrm{g,b} - \phi_\mathrm{p}(z)}{k_\mathrm{B}T}\right) \end{aligned} \tag{5}$$

where k_B is Boltzmann's constant, T is the temperature assumed to be constant over the structure, χ_b is the barrier affinity (all barriers are assumed to be of the same material), $E_{g,b}$ is the barrier bandgap, and $\mathscr{F}_{1/2}$ is the Fermi integral.

It can be seen in Equation 5 that carrier densities are the sum of two terms. The first term is the contribution of discrete states. The second term is an approximation of the contribution of continuum states. It is evaluated assuming a continuous band edge for those states over the quantum-well zone.

2.3.2. Carrier densities in bulk layers

3-D density of states is assumed. Carrier densities are given by the classical expressions:

$$n = N_c \mathscr{F}_{1/2}\left(\frac{\phi_n + \phi - \chi}{k_B T}\right), \qquad p = N_v \mathscr{F}_{1/2}\left(\frac{-\phi + \chi - E_g - \phi_p}{k_B T}\right) \tag{6}$$

2.4. Helmholtz equation

The Helmholtz equation is given by:

$$\Delta E + (k_0^2 \varepsilon_r - \beta^2)E = 0 \tag{7}$$

where E is the optical field and β the modal propagation constant.

The optical permittivity is given by:

$$\varepsilon_r(z) = \bar{n}^2(z) - \alpha_H \frac{\bar{n}(z)}{k_0} g(n,p) + j \frac{\bar{n}(z)}{k_0} g(n,p) \tag{8}$$

where $j^2 = -1$, α_H is the linewidth enhancement factor, $\overline{n}$ is the refractive index, $g(n,p)$ is the local gain and k_0 is the wave vector at the emission wavelength.

2.5. Photon rate equation

The photon rate equation is given by:

$$v_g\left(2\ \mathrm{Im}(\beta) - \alpha_{int} + \frac{\log(R)}{L}\right) N_{ph} + \bar{\beta} R_{sp} = 0 \tag{9}$$

where v_g is the group velocity, α_{int} are the intrinsic losses, L is the device length, R is the facet reflectivity, N_{ph} is the photon density, $\bar{\beta}$ is the spontaneous emission factor and R_{sp} is the spontaneous emission rate. It is stressed that the photon rate equation is 1-D integral over the length of the active zone. Thus, N_{ph} and R_{sp} are defined as the 1-D integral over the length of the active zone (perpendicular to the plane of the quantum wells) of the 3-D photonic density and the 3-D spontaneous emission rate.

2.6. Gain

2.6.1. Local gain

As an MQW laser is used, a logarithmic expression of gain [3] is assumed:

$$g_l(n,p) = a \ln\left(\frac{\min(n,p)}{n_t}\right)$$

where a is the characteristic gain and n_t is the transparency density.

2.6.2. Gain compression

Gain compression is introduced using the gain compression factor ε_s, giving for the actual expression of the local gain:

$$g(n) = \frac{g_l(n,p)}{1 + \varepsilon_s \widetilde{N}_{ph}} \tag{10}$$

where $\widetilde{N}_{ph}$ is the 3-D photon density evaluated assuming $\widetilde{N}_{ph} = N_{ph}|E|^2$ where $|E|^2$ is the normalized 1-D optical field.

2.7. Light output power

Taking into account the axial intensity profile along the longitudinal direction, light output power is given by [4]:

$$P_{out} = v_g \hbar\omega w \frac{1-R}{2\sqrt{R}} N_{ph} \tag{11}$$

where $\hbar\omega$ is the photon energy at the emission wavelength, w is the width of the active zone and R is the reflection coefficient assumed to be equal for both facets of the laser.

2.8. Total current

As a longitudinal variation of N_{ph} is assumed in Equation 11, a similar variation of current must be assumed in order to remain consistent. Therefore the following expression for the total current is assumed:

$$I = JLw \frac{1-R}{\ln(1/R)\sqrt{R}} \tag{12}$$

where J is the 1-D current density and L is the length of active zone.

3. Numerical procedure

3.1. Discretization

The Poisson and Schrödinger equations are discretized within a first-order finite element scheme. The Poisson equation is solved using a Newton–Raphson procedure, where the off-diagonal terms in the derivative matrix are neglected [5].

The Schrödinger equation is solved using the bisection method for eigenvalues and inverse iteration for eigenvectors. For numerical efficiency, discretization of the Schrödinger equation is performed on a restricted zone of the structure chosen to include the quantum wells and the tails of the localized wavefunctions. This zone corresponds to the domain represented in Fig. 2. Details on the solution of this equation can be found in [6].

The transport equations are discretized using the box method, ensuring total current conservation through the whole structure. An ohmic contact is assumed for the boundary condition. Transport equations are solved using a Newton–Raphson procedure. More details on the Poisson and transport equations solutions can be found in [7].

The Helmholtz equation is discretized within the finite-element scheme and solved with an inverse iteration method (fundamental mode only). Neumann boundary conditions are assumed for the optical field.

3.2. Solution of the coupled equations by an iterative procedure

The coupled equations described in Section 2 are solved together by use of a Sharfetter Gummel scheme. In this scheme the potential ϕ is the main variable for the Poisson

equation, the quasi-Fermi levels ϕ_n and ϕ_p for the transport equation, the propagation constant β for the Helmholtz equation and the photon density N_{ph} for the photon rate equation.

An initial solution is obtained by solving the Poisson–transport equations without stimulated recombination. That solution is then used to solve the complete set of equations.

The basic principle of the iteration procedure is presented in Fig. 1. The innermost loops are constituted by the Poisson and Schrödinger equations on the one hand and the transport equations on the other. In the first loop the Poisson and Schrödinger equations were tightly linked in order to prevent algorithm destabilization. Each new equation introduced in the system adds another loop. This is the case for the Helmholtz equation and the photon rate equation; the latter gives the most external loop of the algorithm.

To prevent destabilization or oscillation of the coupled algorithm, relaxation has to be incorporated in the scheme, especially for solving the Poisson–Schrödinger and transport equations. Convergence of a single loop on one variable may indeed induce destabilization of another loop or both. To prevent this, a damping coefficient is used when calculating the derivatives for the Newton–Raphson procedure and a tight control of the number of iterations of each loop.

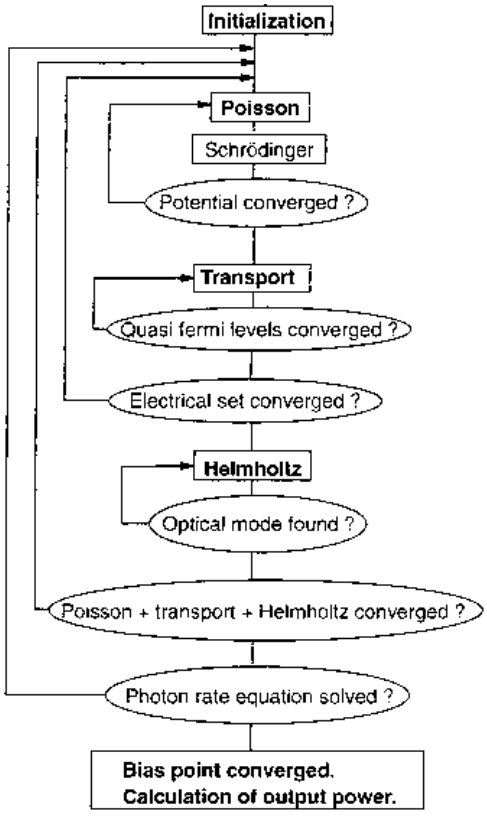

Figure 1 Principle of iterative procedure.

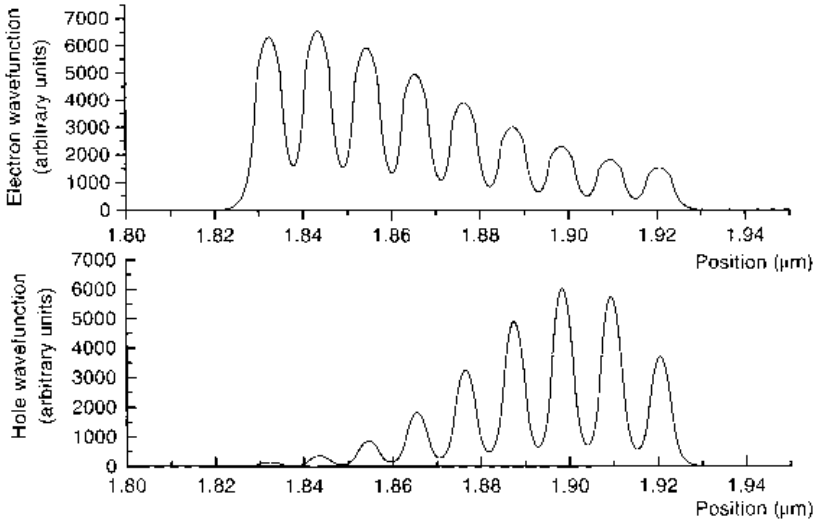

Figure 2 First-level wavefunctions.

These mechanisms, once properly tuned, allowed both convergence with standard criterion convergence and reduction of computation time. For example, computation in the case presented in Fig. 2 (full model – see below) takes about 1 h on an HP j210 workstation.

4. Application to an MQW InGaAs/InGaAsP laser

Our model is used to simulate a nine-well MQW laser fabricated in our laboratory. The material of the quantum wells is $In_{0.47}Ga_{0.53}As$. The material of the barriers is InGaAsP lattice matched on InP ($\lambda_{gap} = 1.2\,\mu m$). The material of the cladding layers in InP. The thickness of the wells is 50 Å and of barriers 60 Å. The quantum-well zone is surrounded by a separate confinement layer of 300 Å on the p-side and 900 Å on the n-side. Doping concentration is 0.5×10^{18} cm^{-3} for the p-side and 1×10^{18} cm^{-3} for the n-side. See Appendix 1 for other parameters.

In that structure, the quantum wells are tightly coupled by thin barriers. This is illustrated by Fig. 2 where the electron wave function of the lowest discrete energy level and the hole wave function of the highest discrete energy level in the wells are plotted. Coupling is shown through a significant probability density $|\psi|^2$ in the barrier.

Figure 3 shows three light-intensity (or L-I) curves: the experimental curve, the numerical curve obtained by the model presented in Section 2 and the numerical curve obtained by the same model and parameters except that the Schrödinger equation was removed from the equation set and the carrier densities were calculated with Equation 6 in all layers. Results are commented on below. Also discussed is how the results differ from those of simple models commonly used for semiconductor lasers.

4.1. Slope of the L-I curve

In semiconductor lasers the slope of the L-I curve at threshold may be given by

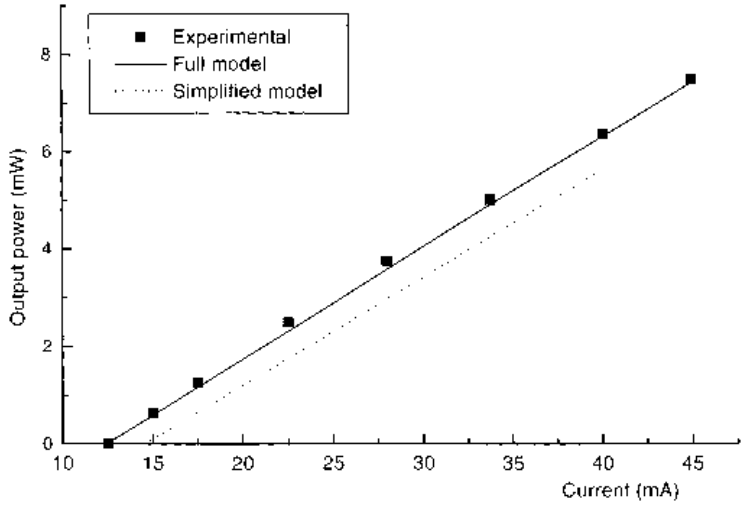

Figure 3 Light-intensity curves.

$$\frac{\mathrm{d}P}{\mathrm{d}I} = \frac{1}{2}\frac{\hbar\omega}{q}\frac{1}{1-\alpha_i\dfrac{L}{\ln R}} \tag{13}$$

The value of α_i was chosen so that this simple model should fit the experimental data, over a wide range of L values. This method of choosing α_i is consistent with our model because integrating Equation 2 leads to the approximate relation:

$$j - j_{\mathrm{th}} = qv_{\mathrm{g}}N_{\mathrm{ph}}\left(\alpha_i - \frac{\ln(R)}{L}\right) \tag{14}$$

and using Equation 14 with Equations 11 and 12 gives Equation 13. Thus, in our example with $L = 210\,\mu\mathrm{m}$ and $\alpha_i = 45\ \mathrm{cm}^{-1}$ a good agreement is found between computation and experimental data. This high value of intrinsic losses is nevertheless standard for this type of quantum-well laser which has a large number of wells leading to a large number of layer interfaces in the active zone and a relatively high confinement factor. Intrinsic losses, which mainly take place in the active zone, are therefore enhanced when compared, for instance, with those of a single quantum-well laser.

Above threshold, for large current values, the experimental data show light saturation that is not taken into account by our model, even if light saturation is present through Equation 10. In our example, experimental output power is lower by 0.5 mW than calculated output power at about 80 mA, that is more than six times the threshold current.

In order to match the experimental light power saturation with Equation 10, a gain compression coefficient would have to be taken which is at least four times larger than was taken for the simulation, leading to a value larger than the commonly accepted values. Therefore gain compression is discarded as the only mechanism to explain light saturation. Thermal effects due to experimental conditions are also discarded. Accordingly, we attribute the difference between computation and experiment to other mechanisms not included in our 1-D model. For instance, the model cannot take into account effects such as lateral current losses or lateral inhomogeneities of carrier densities.

4.2. Threshold current

The stimulated recombination at threshold is negligible and with the 1-D model the threshold current is evaluated with Equation 3:

$$I_{\text{th}} = qwL \int_z (U_{\text{RSH}} + U_{\text{sp}} + U_{\text{Auger}})\text{d}z \tag{15}$$

If it is supposed that carriers are evenly distributed in the wells and close to their mean value, then carrier densities may be considered as independent of z and Equation 15 results in:

$$I_{\text{th}} = qV(U_{\text{RSH}} + U_{\text{sp}} + U_{\text{Auger}}) = qV(An + Bnp + Cnp(n + p)) \tag{16}$$

where V is the active zone volume, and n and p are the average carrier densities for electrons and holes. Coefficients A, B and C account for RSH recombination, spontaneous recombination and Auger recombination respectively. Furthermore, the threshold density can be evaluated by assuming $n = p$ and solving:

$$\Gamma g(n_{\text{th}}) = \alpha_{\text{int}} - \frac{\ln R}{L} \tag{17}$$

where Γ is the optical confinement factor evaluated without carrier injection. It is shown here that this assumption is erroneous for MQW lasers and may result in large mis-evaluation of the threshold current.

The threshold current is a very sensitive parameter especially to the RSH, Auger and spontaneous recombination coefficients whose values are still under discussion for MQW lasers. Consequently, good agreement between experimental value and simulation may be found for both models using parameter values in the commonly accepted range. However, different models, using the same set of parameters, may give very different values for the threshold current as shown in Table I.

The difference between the full model and the simplified model can be explained through the way of estimating carrier densities in the quantum-well zone: 2-D Fermi statistics in the full model and 3-D Fermi statistics in the simplified model. In particular, the same propagation constant is needed to satisfy Equation 9. However, at threshold, as we evaluate carrier density differently, we obtain the same propagation constant by two different carrier density profiles (Fig. 4). Therefore, the recombination rate profile is greatly affected. To illustrate this, Fig. 5 shows the Auger recombination profile for both models. As threshold current is mainly due to recombination currents, a large difference is found between the different models.

This shows that carrier profile in the quantum wells has great importance for MQW laser simulation, because it can lead to a mis-evaluation of the threshold current, by about +15% in our example.

TABLE I Threshold current: experimental and computed values

Experimental value	$I_{\text{th}} = 12.5$ mA
Full model (Section 2)	$I_{\text{th}} = 12.4$ mA
Simplified model (no Schrödinger)	$I_{\text{th}} = 14.5$ mA
Equations 16 and 17 with $\Gamma = 8.14 \times 10^{-2}$ and $n = p = n_{\text{th}} = 4.1 \times 10^{18}$ cm^{-3}	$I_{\text{th}} = 10.8$ mA

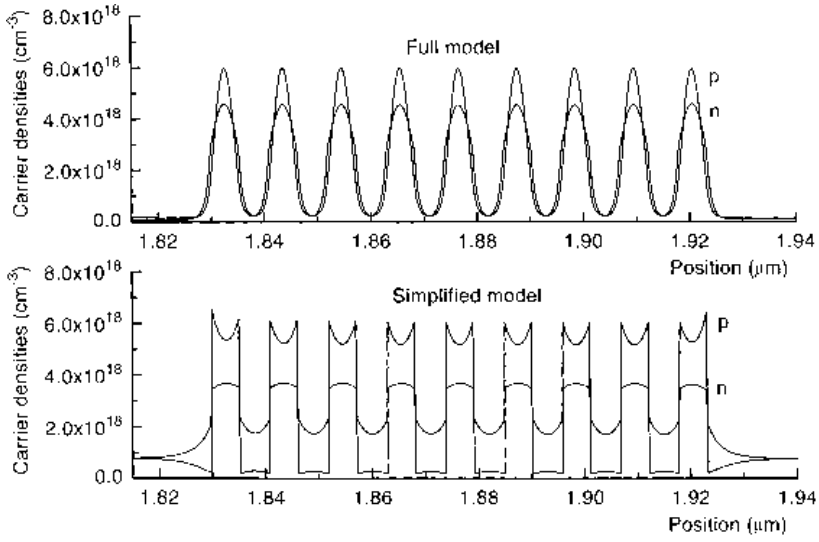

Figure 4 Comparison of carrier densities in quantum-well zone.

The full model can be applied whatever the coupling between wells. In can be particularly applied to other structures with wider barriers. In that case, well-to-well coupling might disappear leading to a possible simplification of the model as the Schrödinger equation needs only to be independently solved in each well. However, in that case, the full model can still be used. For example, a similar analysis was performed on an eight-well lattice-matched GaInAs/GaInAsP/InP quantum-well laser with identical well and barrier width (100 Å) leading to analogous results.

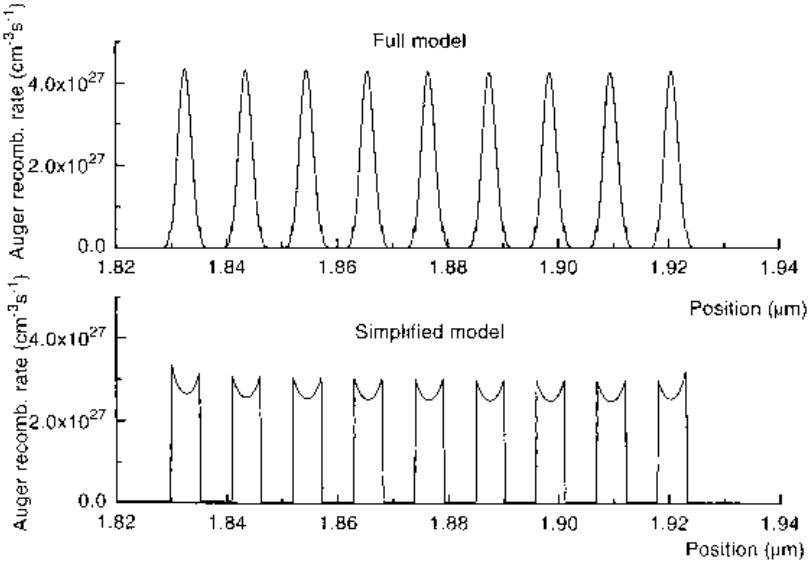

Figure 5 Comparison of Auger recombination rate in quantum-well zone.

5. Conclusion

A self-consistent model has been presented for 1-D MQW laser simulation, which takes into account both band bending and coupling in quantum wells through the Schrödinger equation. The computed L-I curve has been compared with experimental results and a good agreement has been found near threshold, for a given set of parameters. However, our computations cannot achieve a predictive ability due to uncertainties on the parameters, such as the recombination coefficients.

Nevertheless, the comparison between our quantum model, which rigorously deals with the quantum-well zone, and simplified models shows a large difference in the spatial carrier density profile. This has important consequences on spatial carrier recombination rate profiles and hence on the estimate of the threshold current.

We expect that our rigorous treatment of the quantum-well zone has important consequences on other fundamental parameter modelling for MQW lasers, such as the differential gain. This will be the subject of future work.

Acknowledgement

We thank I. Abram for a critical reading of the manuscript.

References

1. ZHAN-MING LI, KENNETH M. DZURKO, ANDRÉ DELÂGE and SEAN P. McALISTER, *IEEE J. Quantum Electron.* **4** (1992) 792.
2. NIR TESSLER and GADI EISENSTEIN, *IEEE J. Quantum Electron.* **6** (1993) 1586.
3. T. A.-MA, Z. M. LI, T. MAKINO and M. S. WARTAK, *IEEE J. Quantum Electron.* **1** (1995) 29.
4. K.J. EBELING, in *Integrated Opto-Electronics* (Springer-Verlag 1993) Ch. 10, 318.
5. I.-H. TAN, G. L. SNIDER, L. D. CHANG and E. L. HU, *J. Appl. Phys.* **8** (1990) 4071.
6. F. STERN and S. DAS SARMA, *Phys. Rev. B* **30** (1984) 840.
7. E. CAQUOT, J. DANGLA, M. CAMPANA, D. ANKRI and J. F. PALMIER, *Proc. ESSDERC 1984* (North-Holland, Amsterdam, 1985) p. 356.

Appendix 1 Main numerical parameters used in simulation

Parameter	Symbol and value
Intrinsic losses	$\alpha_{\text{int}} = 45\ \text{cm}^{-1}$
Facet reflectivity	$R = 0.31$
Gain parameters for logarithmic expression	$g = a \ln\left(\frac{n}{n_t}\right)$
	$a = 1342\ \text{cm}^{-1},\ n_t = 1.5 \times 10^{18}\ \text{cm}^{-3}$
Gain compression coefficient	$\varepsilon_s = 5 \times 10^{-17}\ \text{cm}^{-3}$
Henry's factor	$\alpha_H = 3.5$
Group index	$n_g = 3.8$
RSH coefficient	$A = 2.5 \times 10^{8}\ \text{s}^{-1}$
Spontaneous recombination coefficient	$B = 1 \times 10^{-10}\ \text{cm}^3\ \text{s}^{-1}$
Auger coefficient	$C = 1.5 \times 10^{-29}\ \text{cm}^6\ \text{s}^{-1}$
Emission wavelength	$\lambda = 1.55\ \mu\text{m}$